Non intrusive method for parametric model order reduction using a bi-calibrated interpolation on the Grassmann manifold

M. Oulghelou, C. Allery

Version of Record: https://www.sciencedirect.com/science/article/pii/S0021999120306987
Manuscript_5c4071a126aad5858f6d25f23290166c

Non intrusive method for parametric model order reduction using a bi-calibrated interpolation on the Grassmann manifold

M. Oulghelou[1], C. Allery[2]

LaSIE, UMR-7356-CNRS, Université de La Rochelle Pôle Science et Technologie, Avenue Michel Crépeau, 17042 La Rochelle Cedex 1, France.

Abstract

Approximating solutions of non-linear parametrized physical problems by interpolation presents a major challenge in terms of accuracy. In fact, pointwise interpolation of such solutions is rarely efficient and generally leads to incorrect predictions. To overcome this issue, instead of interpolating solutions directly by a straight forward approach, reduced order models (ROMs) can be efficiently used. To this end, the ITSGM (Interpolation On a Tangent Space of the Grassmann Manifold) is an efficient technique used to interpolate parameterized POD (Proper Orthogonal Decomposition) bases. The temporal dynamics is afterwards determined by the Galerkin projection of the predicted basis onto the high fidelity model. However, such interpolated ROMs based on ITSGM/Galerkin are intrusive, given the fact that their construction requires access to the equations of the underlying high fidelity model. In the present paper a non-intrusive approach (Galerkin free) for the construction of reduced order models is proposed. This method, referred to as Bi-CITSGM (Bi-Calibrated ITSGM) consists of two major steps. First, the untrained spatial and temporal bases are predicted by the ITSGM method and the POD eigenvalues by spline cubic. Then, two orthogonal matrices, determined as analytical solutions of two optimization problems, are introduced in order to calibrate the interpolated bases with their corresponding eigenvalues. Results on the flow problem past a circular cylinder where the parameter of interpolation is the Reynolds number, show that for new untrained Reynolds number values, the developed approach produces sufficiently accurate solutions in a real-computational time.

Keywords: Non-intrusive Reduced Order Models (ROMs), Proper Orthogonal Decomposition (POD), bases interpolation, Grassmann manifold.

[1]mourad.oulghelou@univ-lr.fr
[2]cyrille.allery@univ-lr.fr

1. Introduction

Parametrized physical problems arise in many practical engineering design and analysis problems such as aerospace engineering [1, 2], biomedical engineering [3], flow control [4] etc. The numerical computational cost of these applications can be exorbitant. Particularly, for applications requiring multiple resolutions of the high fidelity model over the parameter space, using a fine spatial mesh and small time-steps. For complex non-linear physical phenomena, even with modern computers, these numerical computations still remain time-consuming. Besides numerical computations, experiments can be carried out. Nevertheless, these last remain expensive as well. In order to computationally tackle these challenging cost issues, reduced order models, allowing to represent the solutions in a much lower dimensional subspace that contain the mean features of the original system, can be used. Such techniques lead to significant computational cost savings, especially in applications requiring multiple evaluations of the solution over the parameter space [5, 6, 7].

The Proper Orthogonal decomposition (POD) method is the most used method for reducing problems dimensionality. Starting from a set of available snapshot solutions at different instants, the POD method aims at constructing a subspace (represented by a set of basis functions) where each snapshot solution can be accurately represented. The most striking property of POD is its optimality [8]. This means that the POD basis is the lowest rank possible basis that captures the quasi-totality of the information initially contained in the set of snapshots. It is simply formed by considering the modes carrying high energy contributions. Once the truncated POD basis is available, the temporal dynamics can be determined by solving a low order system obtained from the Galerkin projection of this basis onto the high fidelity model[9]. Nevertheless, a POD basis is optimal only for the solution snapshots considered for its construction. Consequently, using this basis to predict the ROM for a different parameter value often results in solutions lacking accuracy.

To overcome this issue, it is possible to use the ITSGM (Interpolation on Tangent spaces of the Grassmann Manifold) method based on the tools of differential geometry. This powerful method was firstly introduced by Amsallem et al. [10] in the context of aeroelasticity and applied successfully in sub-optimal control of transfer phenomena [11, 12]. Consider an ensemble of distinct trained parameters for which a set of POD spatial bases of the same dimension is available. These bases can be seen as representatives of points on the Grassmann manifold which can be connected by geodesic paths (second order ordinary differential equations). By choosing a reference point[3], one can notice that the geodesic paths connecting this last to the other sampling points can be distinguished only by their initial velocities. Given that these velocities belong to the tangent space at the reference point which is a flat space, they can be easily interpolated for a new untrained parameter value in order to predict the corresponding untrained spatial basis and then construct the interpolated ROM via the Galerkin projection. Eventhough its effectiveness, this approach and others based on Galerkin projection suffer from intrusiveness, thus the necessity to access to the underlying mathematical problem.

This provided us a key motivation for the development of an alternative non intrusive reduced order model technique. In the context of non intrusive model reduction, Xiao et al. [13, 14] suggest an approach using a two-level RBF interpolation to study the two dimensional flow around a cylinder when the Reynolds number varies. Another approach proposed by Shinde et al. [15] suggests to simply approximate the spatial and temporal bases functions by linearly interpolating their modes. This approach was also applied by Joyner [16] for eddy current damage detection.

In the present article, we propose a novel non-intrusive model reduction method addressed to approximate time-dependent parametrized non-linear physical phenomena. Being inspired

[3]The reference point is the subspace represented by an arbitrary chosen POD basis from sampling.

from ITSGM, the new model reduction method is called throughout the paper Bi-CITSGM (Bi-Calibrated Interpolation on Tangent spaces of the Grassmann Manifold). In contrast to ITSGM/Galerkin, the Bi-CITSGM does not require access to the underlying mathematical model. It is based on data and can be applied to generalized parametrized non-linear physical phenomena. The solutions data can either be provided by numerical computations or experimental observations. Let us consider an ensemble of solution snapshots obtained from experiment or from solving the high fidelity model at a finite set of trained points in the parameter space. The Bi-CITSGM is carried out in two phases, an offline phase and an online phase. The offline phase is the one of data processing where each ensemble of snapshots is represented in a low dimensional subspace through the POD method. The online phase corresponds to the process of interpolation and calibration. It consists first in interpolating the POD eigenvalues by using spline cubic; then to predict the spatial and temporal bases by using the ITSGM method; and finally, to introduce two small sized matrices serving to calibrate the spatial and temporal modes with the interpolated eigenvalues. These undetermined calibration matrices obey the orthonormality condition and are determined as the solution of two separate optimization problems.

The remainder of the paper is organized as follows: First, a brief overview of Geodesic paths parametrization on the Grassmann manifold is given in section 2. In section 3, we outline the bases interpolation problem and recall the ITSGM method. Then , the new proposed non intrusive approach Bi-CITSGM is formalized in section 4 and application to the parametrized flow past a circular cylinder is given in Section 5. Finally, conclusions are drawn in Section 6.

2. Review of the Grassmann manifold

Recently, the Grassmann manifold has attracted great interest in various applications, such as subspace tracking [17], sparse coding [18, 19], clustering [20], model reduction [10, 12], etc. The Grassmann manifold $\mathcal{G}(q,N)$ is defined as the set of all q-dimensional subspaces in $\mathbb{R}^N$, where $0 \leq q \leq N$. It is a matrix manifold that is locally similar to an Euclidean space around each of its points. A concrete representation of the Grassmann manifold is the Stiefel Manifold representation [21] given as

$$\mathcal{G}(q,N) \cong \mathcal{ST}(q,N)/\boldsymbol{\mathcal{O}}(q)$$

where $\boldsymbol{\mathcal{O}}(q)$ is the group of all $q \times q$ orthogonal matrices and $\mathcal{ST}(q,N) = \{\varphi \in \mathbb{R}^{N\times q} : \varphi^T\varphi = I_q\}$ the set of all bases of dimension q, called Stiefel manifold [21, 22]. A point $[\varphi] \in \mathcal{G}(q,N)$ is defined by

$$[\varphi] = \{\varphi Q \mid \varphi^T\varphi = I_q, \quad Q \in \boldsymbol{\mathcal{O}}(q)\}$$

where $[\varphi]$ is realized as a representative of the equivalence class $\{\varphi Q : \text{ for all } Q \in \boldsymbol{\mathcal{O}}(q)\}$. At each point $[\varphi]$ of the manifold $\mathcal{G}(q,N)$, a tangent space [21, 22] of the same dimension [21] can be defined by the following abstract concrete set [23]

$$\mathcal{T}_{[\varphi]}\mathcal{G}(q,N) = \{\mathcal{X} \in \mathbb{R}^{N\times q} \mid \quad \varphi^T\mathcal{X} = 0\}.$$

The geodesic distance $dist_{\mathcal{G}}(\varphi, \Psi)$ between two points $[\varphi]$ and $[\Psi]$ of the Grassmann manifold is the minimum of paths lengths between them. By taking the SVD (Singular Value Decomposition) of $\varphi^T\Psi$ as $U\Sigma V^T = \varphi^T\Psi$ such that $\Sigma = \text{diag}(\sigma_i)$, the geodesic distance between $[\varphi]$ and $[\Psi]$ is defined as the summation of squared principal angles

$$dist_{\mathcal{G}}(\varphi, \Psi) = \sqrt{\sum_i \arccos^2(\sigma_i)} \tag{1}$$

A path that minimizes this distance is called geodesic [24]. This path is associated with a

second order differential equation [22, 21, 25] uniquely defined by two initial conditions : the initial position and initial velocity [24]. A geodesic path can then be represented by a twice differentiable function $\Gamma : [0,1] \longrightarrow \mathcal{G}(q,N)$, where $\Gamma(0)$ and $\Gamma(1)$ are respectively its initial and final points. The parametric representation of the geodesic path in $\mathcal{G}(q,N)$ with initial conditions $\Gamma(0) = [\varphi]$ and $\dot{\Gamma}(0) = \mathcal{X}$ is given by [22, 21]

$$\Gamma(t) = \text{span}\left\{\varphi V \cos(t\Sigma) + U \sin(t\Sigma)\right\} \qquad 0 \leq t \leq 1 \tag{2}$$

where $U\Sigma V^T$ is the thin SVD of the initial velocity $\mathcal{X}$. For every point $[\varphi]$ in $\mathcal{G}(q,N)$ there exists a unique geodesic starting from $[\varphi]$ in every direction $\mathcal{X} \in \mathcal{ST}(q,N)$, giving us the exponential map $\text{Exp}_{[\varphi]} : \mathcal{T}_{[\varphi]}\mathcal{G}(q,N) \longrightarrow \mathcal{G}(q,N)$ explicitly calculated as $\text{Exp}_{[\varphi]}(\mathcal{X}) = \Gamma(1) = [\Psi]$. The exponential of $\mathcal{X}$ is given by

$$[\Psi] = \text{span}\{\varphi V \cos(\Sigma) + U \sin(\Sigma)\} \tag{3}$$

Let us denote $\text{Log}_{[\varphi]}$ the inverse map of $\text{Exp}_{[\varphi]}$, which is defined only in a certain neighbourhood of $[\varphi]$. If $\text{Exp}_{[\varphi]}(\mathcal{X}) = [\Psi]$, then $\mathcal{X}$ is the vector

$$\mathcal{X} = \text{Log}_{[\varphi]}([\Psi]) = U \arctan(\Sigma) V^T \tag{4}$$

with $U\Sigma V^T$ is the thin SVD of $(I - \varphi\varphi^T)\Psi(\varphi^T\Psi)^{-1}$ and $\text{Log}_{[\varphi]}([\varphi]) = 0$

3. Subspaces interpolation using ITSGM method

Let $\{\theta_i \in \mathbb{R}^p, i = 1, \cdots, N_p\}$ be a set of parameters and $[\varphi_{\theta_1}], [\varphi_{\theta_2}], \ldots, [\varphi_{\theta_{N_p}}]$ the corresponding set of N_p parametrized subspaces [4] belonging to $\mathcal{G}(q,N)$. Consider the problem of interpolation in which we seek an approximation of $[\varphi_{\widetilde{\theta}}]$ for an untrained parameter $\widetilde{\theta} \notin \{\theta_1, \ldots, \theta_{N_p}\}$. Provided that the Grassmann manifold is not a flat space, straight forward interpolation of its points does not necessarily result in a point that is included in it. Therefore, it is necessary to reformulate the interpolation process to be suitable for points in the Grassmann manifold. To provide a well defined interpolation framework of points in the Grassamnn manifold, Amsallem et al. proposed the ITSGM (Interpolation on a Tangent space of the Grassmann Manifold) [10]. It consists in the following steps

step 1 Choose the origin point of tangency, for example $[\varphi_{\theta_{i_0}}]$ where $i_0 \in \{1, \ldots, N_p\}$.

step 2 For $i \in \{1, \ldots, N_p\}$, map the point $[\varphi_{\theta_i}] \in \mathcal{G}(q,N)$ to $\mathcal{X}_i \in \mathcal{T}_{[\varphi_{i_0}]}\mathcal{G}(q,N)$ such that $\mathcal{X}_i = \text{Log}_{[\varphi_{\theta_{i_0}}]}(\varphi_{\theta_i})$ is the vector represented by

$$\mathcal{X}_i = U_i \arctan(\Sigma_i) V_i^T$$

where $U_i\Sigma_i V_i^T = (I - \varphi_{\theta_{i_0}}\varphi_{\theta_{i_0}}{}^T)\varphi_{\theta_i}(\varphi_{\theta_{i_0}}{}^T\varphi_{\theta_i})^{-1}, i = 1, \ldots, N_p$, are thin SVD.

step 3 Interpolate the initial velocities $\mathcal{X}_1, \mathcal{X}_2, \ldots, \mathcal{X}_{N_p}$ for the untrained parameter $\widetilde{\theta}$ using a standard interpolation and obtain $\mathcal{X}_{\widetilde{\theta}}$.

step 4 Finally by the exponential mapping, map the interpolated velocity $\mathcal{X}_{\widetilde{\theta}}$ back to the Grassmann manifold. The matrix representation of the interpolated subspace is given by

$$\varphi_{\widetilde{\theta}} = \varphi_{\theta_{i_0}} \widetilde{V} \cos(\widetilde{\Sigma}) + \widetilde{U} \sin(\widetilde{\Sigma})$$

where $\widetilde{U}\widetilde{\Sigma}\widetilde{V}^T$ is the thin SVD of the initial velocity vector $\mathcal{X}_{\widetilde{\theta}}$.

An illustration of the ITSGM is given in B.1. For more details the reader can refer to Amsallem et al. [10] and Absil et al. [22].

[4] Here φ_{θ_i} is refereed to as a possible representative basis of the subspace $\varphi_{\theta_i} \in \mathcal{G}(q,N)$. Typically, this basis can be a POD basis associated to the parameter θ_i.

4. Bi-CITSGM method

4.1. Problem statement

Given a set of parameter values $\{\theta_i \in \mathbb{R}^p, i = 1, \cdots, N_p\}$ for which we dispose of N_p solutions at N_s different time instants of a discretized time dependent non-linear parametrized physical problem of size N_x. By assuming that these parametrized solutions are stored in $N_x \times N_s$ matrices $\boldsymbol{S}_{\theta_i}$, the aim is to approximate the solution snapshots matrix $\boldsymbol{S}_{\widetilde{\theta}}$ for a new untrained parameter value $\widetilde{\theta} \notin \{\theta_1, \ldots, \theta_{N_p}\}$ without going through costly numerical or experimental procedures. A trivial approach to solve this problem is to use standard interpolation approaches such as Lagrange, RBF (Radial Basis Function), IDW (Inverse Distance weighted), etc. These methods are known to be efficient for linear or weakly non-linear problems, while for non-linear phenomena, they are pointless and unuseful. To overcome this limitation we introduce in the following a new interpolation approach based on the ITSGM. This approach is referred to as Bi-CITSGM (Bi-Calibrated Interpolation on Tangent spaces of the Grassmann manifold).

4.2. Description of the method

Let us assume that $\boldsymbol{S}_{\theta_i}$ is approximated in the low dimensional subspace $[\varphi_{\theta_i}]$ calculated by the POD method [5] as follows

$$\boldsymbol{S}_{\theta_i} \approx \varphi_{\theta_i} \Sigma_{\theta_i} {\Lambda_{\theta_i}}^T, \quad i = 1, \ldots, N_p, \tag{5}$$

where $\Sigma_{\theta_i} \in \mathbb{R}^{q \times q}$ is the matrix of singular values (square roots of POD eigenvalues) of $\boldsymbol{S}_{\theta_i}$, and $\varphi_{\theta_i} \in \mathcal{ST}(q, N_x)$ and $\Lambda_{\theta_i} \in \mathcal{ST}(q, N_s)$, $i = 1, \ldots, N_p$, are the corresponding spatial and temporal bases.

For a new untrained parameter value $\widetilde{\theta} \notin \{\theta_1, \ldots, \theta_{N_p}\}$, the first step of the Bi-CITSGM method is to approximate the matrix of singular values $\Sigma_{\tilde{\theta}}$ by spline cubic interpolation[6]. Next, by using the ITSGM method, the sampling subspaces $[\varphi_{\theta_i}]$ (resp. $[\Lambda_{\theta_i}]$) are interpolated and an approximated subspace $[\varphi_{\tilde{\theta}}]$ (resp. $[\Lambda_{\tilde{\theta}}]$) is obtained. Since $\varphi_{\tilde{\theta}}$ and $\Lambda_{\tilde{\theta}}$ are only two possible representatives of the subspaces $[\varphi_{\tilde{\theta}}]$ and $[\Lambda_{\tilde{\theta}}]$, the right classification of modes according to the interpolated POD eigenvalues is not necessarily verified. Thus, the approximated snapshots matrix $\boldsymbol{S}_{\tilde{\theta}}$ must be calibrated as follows

$$\boldsymbol{S}_{\tilde{\theta}} = \varphi_{\tilde{\theta}} Q_x \Sigma_{\tilde{\theta}} Q_t^T {\Lambda_{\tilde{\theta}}}^T$$

where $Q_x, Q_t \in \mathcal{O}(q)$[2] are introduced to recover the POD character of $\varphi_{\tilde{\theta}}$ and $\Lambda_{\tilde{\theta}}$ respectively. These two matrices are of a big significance in the expression of $\boldsymbol{S}_{\tilde{\theta}}$. In fact, their introduction guarantees the adequate combination of column vectors of $\varphi_{\tilde{\theta}}$ and $\Lambda_{\tilde{\theta}}$ which realizes the best fit with the interpolated singular values matrix $\Sigma_{\tilde{\theta}}$. The question of finding the best calibration matrices Q_x and Q_t is a delicate one. In the following we propose a practical approach where these matrices are obtained as the analytical solutions of two optimization problems.

First of all, the modes orientation of the sampling spatial and temporal bases must be adjusted with respect to a reference basis [7]. The reference basis denoted $\varphi_{\theta_{k_0}}$, is chosen as the closest basis to $\varphi_{\tilde{\theta}}$ in the sense of the Grassmannian distance. Thus, k_0 is determined by

$$k_0 = \underset{i \in \{1, \ldots, N_p\}}{\mathbf{argmin}} \; dist_{\mathcal{G}}(\varphi_{\tilde{\theta}}, \varphi_{\theta_i})$$

[5] The POD basis can be chosen to be optimal with respect to any inner product, namely, L^2 or H^1 or Euclidean inner product. For the sake of simplicity, the Euclidean 2-norm is used in the following.

[6] Other interpolation techniques can be used, typically Lagrange, RBF, IDW, etc

[7] In this manipulation, orientations of spatial and temporal modes are simultaneously adjusted. For example, the j^{th} modes associated to φ_{θ_k} and Λ_{θ_k} can be multiplied by -1, without causing any effect on the snapshot matrices representation given by (5).

Denote by $||\cdot||_2$ the Euclidean two-norm. Once $\varphi_{\theta_{k_0}}$ is known, the modes orientation adjustment is performed by algorithm 1.

Algorithm 1: Bases modes orientation adjustment.

```
for k = 1, ..., N_p do
    for j = 1, ..., q and j ≠ j_0 do
        If ||φ_{θ_{k_0}}^j − φ_{θ_k}^j||_2 > ||φ_{θ_{k_0}}^j + φ_{θ_k}^j||_2
            multiply the j^th spatial and temporal modes φ_{θ_k}^j and Λ_{θ_k}^j by −1.
    end
end
```

The steps of determining Q_x and Q_t are the same. The methodology is then described only for the finding of the spatial calibration matrix Q_x, the same applies to the determination of Q_t. The spatial calibration matrix Q_x is sought as the solution of the constrained minimization problem

$$\min_{Q_x \in \mathcal{O}(q)} \sum_{i=1}^{N_p} \omega_i ||\varphi_{\tilde{\theta}} Q_x - \varphi_{\theta_i}||_F^2 \tag{6}$$

where $||\cdot||_F$ is the Frobenius norm and ω_i are the weights given for $m > 1$ by

$$\omega_i = \frac{dist_{\mathcal{G}}(\varphi_{\tilde{\theta}}, \varphi_{\theta_i})^{-m}}{\sum_{k=1}^{N_p} dist_{\mathcal{G}}(\varphi_{\tilde{\theta}}, \varphi_{\theta_k})^{-m}} \tag{7}$$

The Lagrange function associated to the constrained minimization problem (6) writes

$$\mathcal{L}(Q_x, R) = \sum_{i=1}^{N_p} \omega_i ||\varphi_{\tilde{\theta}} Q_x - \varphi_{\theta_i}||_F^2 + \text{Trace}\left[R(Q_x^T Q_x - I_q)\right]$$

where R is a symmetric matrix referred to as the "Lagrange multiplier". Considering the fact that $\omega_1 + \cdots + \omega_{N_p} = 1$, the Lagrange function simplifies to

$$\begin{aligned}\mathcal{L}(Q_x, R) &= \sum_{i=1}^{N_p} \omega_i ||\varphi_{\tilde{\theta}} Q_x||_F^2 - 2\sum_{i=1}^{N_p} \omega_i \text{Trace}\left({\varphi_{\theta_i}}^T \varphi_{\tilde{\theta}} Q_x\right) + \sum_{i=1}^{N_p} \omega_i ||\varphi_{\theta_i}||_F^2 + \text{Trace}\left[R(Q_x^T Q_x - I_q)\right] \\ &= \text{Trace}\left[(I_q + R) Q_x^T Q_x\right] - 2\sum_{i=1}^{N_p} \omega_i \text{Trace}\left({\varphi_{\theta_i}}^T \varphi_{\tilde{\theta}} Q_x\right) - \text{Trace}\,(R) + q\end{aligned}$$

Using the following differentiation identities

$$\frac{d}{dB} Trace(AB^T B) = B(A + A^T)$$
$$\frac{d}{dB} Trace(AB) = A^T$$

The differential of $\mathcal{L}$ with respect to Q_x yields

$$\partial_{Q_x} \mathcal{L}(Q_x, R) = 2Q_x(I_q + R) - 2{\varphi_{\tilde{\theta}}}^T \sum_{i=1}^{N_p} \omega_i \varphi_{\theta_i} \tag{8}$$

When $\partial_{Q_x} \mathcal{L}(Q_x, R)$ vanishes, Q_x is a stationary point characterized by

$$Q_x\,(I_q + R) = {\varphi_{\tilde{\theta}}}^T \sum_{i=1}^{N_p} \omega_i \varphi_{\theta_i} \tag{9}$$

By considering the SVD decomposition of the matrix

$$\varphi_{\tilde{\theta}}{}^{T} \sum_{i=1}^{N_p} \omega_i \varphi_{\theta_i} = \xi \Theta \eta^T \tag{10}$$

It follows that

$$\left(I_q + R\right)^T Q_x^T Q_x \left(I_q + R\right) = \eta \Theta^2 \eta^T$$

Given that Q_x is orthonormal and that R is symmetric, we can write

$$I_q + R = \eta \Theta \eta^T$$

By plugging the expression of $I_q + R$ into the equation (10), the analytical expression of the spatial calibration matrix Q_x follows

$$Q_x = \xi \eta^T$$

In the same fashion, the temporal calibration matrix Q_t is expressed by

$$Q_t = \zeta \rho^T$$

where ζ and ρ are the left and right singular eigenvectors of the matrix $\Lambda_{\tilde{\theta}}{}^{T} \sum_{i=1}^{N_p} \kappa_i \Lambda_{\theta_i}$ and

$$\kappa_i = \frac{dist_{\mathcal{G}}(\Lambda_{\tilde{\theta}}, \Lambda_{\theta_i})^{-l}}{\sum_{k=1}^{N_p} dist_{\mathcal{G}}(\Lambda_{\tilde{\theta}}, \Lambda_{\theta_k})^{-l}}, \quad l \geq 1 \tag{11}$$

Remark 1. *If the matrix* $A = \varphi_{\tilde{\theta}}{}^{T} \sum_{i=1}^{N_p} \omega_i \varphi_{\theta_i}$ *is singular, we can use SVD to approximate its inverse called pseudo-inverse with the following matrix*

$$A^{-1} \approx A^{+} = \eta \Theta^{+} \xi^T$$

where for a small threshold $\varepsilon > 0$*, the matrix* Θ^{+} *is given by*

$$\Theta^{+} = \begin{cases} 1/\theta_i & \text{if } \theta_i > \varepsilon \\ 0 & \text{otherwise} \end{cases}$$

In this case, the spatial calibration matrix is approximated as follows

$$Q_x \approx \xi I_{Q_x}^{+} \eta^T$$

where

$$I_{Q_x}^{+} = \begin{cases} 1 & \text{if } \theta_i > \varepsilon \\ 0 & \text{otherwise} \end{cases}$$

The same remark apply to approximate the temporal calibration matrix and we have

$$Q_t \approx \zeta I_{Q_t}^{+} \gamma^T$$

where

$$I_{Q_t}^{+} = \begin{cases} 1 & \text{if } \delta_i > \varepsilon \\ 0 & \text{otherwise} \end{cases}$$

The different steps of the Bi-CITSGM method are summarized in algorithm 2.

Algorithm 2: Bi-CITSGM.

Offline:

For each parameter value θ_i, $i = 1, \ldots, N_p$, approximate the snapshots matrix $\boldsymbol{S}_{\theta_i}$ by the POD of order q as follows

$$\boldsymbol{S}_{\theta_i} \approx \varphi_{\theta_i} \Sigma_{\theta_i} {\Lambda_{\theta_i}}^T$$

Online:

Interpolate the singular values matrices $\Sigma_{\theta_1}, \cdots, \Sigma_{\theta_{N_p}}$ and obtain $\Sigma_{\tilde{\theta}}$ the singular value matrix associated to the untrained parameter $\tilde{\theta}$.

Interpolate $[\varphi_{\theta_i}]$ and $[\Lambda_{\theta_i}]$, $i = 1, \ldots, N_p$, by using the ITSGM method and obtain the spatial and temporal bases $\varphi_{\tilde{\theta}}$ and $\Lambda_{\tilde{\theta}}$.

Perform algorithm 1 for modes orientation adjustment.

Calculate the weights ω_i and κ_i using equations (7) and (11).

Perform SVD decompositions

$${\varphi_{\tilde{\theta}}}^T \sum_{i=1}^{N_p} \omega_i \varphi_{\theta_i} = \xi \Theta \eta^T \qquad {\Lambda_{\tilde{\theta}}}^T \sum_{i=1}^{N_p} \kappa_i \Lambda_{\theta_i} = \zeta \delta \rho^T$$

Calculate $I^+_{Q_x}$ and $I^+_{Q_t}$ and evaluate the calibration matrices Q_x and Q_t as follows

$$Q_x = \xi I^+_{Q_x} \eta^T \qquad Q_t = \zeta I^+_{Q_t} \rho^T$$

Reconstruct the interpolated snapshots matrix

$$\boldsymbol{S}_{\tilde{\theta}} = \varphi_{\tilde{\theta}} Q_x \Sigma_{\tilde{\theta}} Q_t^T {\Lambda_{\tilde{\theta}}}^T$$

4.3. Computational complexity

In the case of a univariate interpolation, it was demonstrated in [10] that the computational cost of ITSGM performed on spatial bases is proportional to $\mathcal{O}(N_x q^2)$. Similarly a computational cost proportional to $\mathcal{O}(N_s q^2)$ is expected for temporal bases interpolation. The other operations of the Bi-CITSGM algorithm involve matrix-matrix products and Singular value decompositions. Their total computational cost still proportional to $\mathcal{O}(N_x q^2)$ and $\mathcal{O}(N_s q^2)$. Since in general $N_s \ll N_x$, the complexity of Bi-CITSGM can be approximated as being proportional to $\mathcal{O}(N_x q^2)$. In other words, the complexity is a linear function of the number of degrees of freedom of the underlying higher-order computational model, which makes the Bi-CITSGM method computationally efficient. Furthermore, in the particular case of a linear interpolation, it is possible to drastically reduce the computational cost of Bi-CITSGM by considering the interpolation procedure proposed by Nguyen [26]. In this case, the complexity can reduce to be proportional to $\mathcal{O}(q^3)$.

5. Numerical example : flow past a cylinder

5.1. High fidelity problem

Consider the two dimensional flow past a circular cylinder of diameter D. The problem domain is rectangular with length $H = 30D$ and width $45D$. The center of the cylinder is situated at $L_1 = 10D$ from the left boundary and $H/2$ from the lower boundary. The fluid dynamics of the flow is driven by an inlet velocity U of a unit magnitude, which enters from the left boundary of the domain, and is allowed to flow past through the right

boundary of the domain. Free slip boundary conditions are applied to the horizontal edges whilst no slip boundary condition are considered on the cylinder's wall. The illustration of the flow configuration is given in Figure B.2. The underlying problem is governed by the Navier-Stokes equations

$$\begin{cases} \partial_t \boldsymbol{u} - \dfrac{1}{Re}\Delta \boldsymbol{u} + \boldsymbol{u}\cdot\nabla\boldsymbol{u} + \nabla p = 0 & \text{in } \Omega \times [0,T[\\ \nabla\cdot\boldsymbol{u} = 0 & \text{in } \Omega \times [0,T[\\ \boldsymbol{u} = U & \text{on } \Gamma_{inflow} \times [0,T[\\ \boldsymbol{u} = 0 & \text{on } \Gamma_{noslip} \times [0,T[\\ u_2 = 0 & \text{on } \Gamma_{freeslip} \times [0,T[\\ \partial_{\boldsymbol{n}} u_1 = 0 & \text{on } \Gamma_{freeslip} \times [0,T[\\ -\dfrac{1}{Re}\partial_{\boldsymbol{n}}\boldsymbol{u} + p\boldsymbol{n} = 0 & \text{on } \Gamma_{out} \times [0,T[\\ \boldsymbol{u}(0) = \boldsymbol{u}_0 & \text{in } \Omega \end{cases} \tag{12}$$

The parameter to vary is the Reynolds number $Re = UD/\nu$ ranged from 90 to 450.Numerical simulations were performed with Fenics [27] (Taylor-Hood finite element $\mathbb{P}_2/\mathbb{P}_1$) using the time step 0.01 and the non-uniform mesh represented in figure B.3. This mesh includes 85124 DOFs for velocity and 10694 DOFs for the pressure. In order to validate the high fidelity model, the hydrodynamics coefficients obtained at $Re = 100$ were investigated. These are the mean drag $\overline{C}_D$, the maximum lift value $C_{L,max}$, the root mean square lift value $C_{L,rms}$ and the Strouhal number S_t. Table B.1 compares the present computed coefficients against measurement data and other computation results. It shows a good agreement between literature data and the present simulations. In the following, a solution snapshot of the periodic flow regime at $Re = 100$ is considered as the initial condition to generate the sampling simulations for different training Reynolds number values.

5.2. Construction of the POD sampling bases

The training flows are obtained by solving the high fidelity model [8] for the training Reynolds number values included in $[90, 450]$ where the final time T is equal to 12. The velocity and pressure variables are decomposed into mean and fluctuating parts as follows

$$\begin{cases} \boldsymbol{u}(t,x,Re) = \overline{\boldsymbol{u}}(x) + \boldsymbol{u}'(t,x,Re), & \text{in } \Omega \\ p(t,x,Re) = \overline{p}(x) + p'(t,x,Re), & \text{in } \Omega \end{cases}$$

The mean parts $\overline{\boldsymbol{u}}$ and $\overline{p}$ are given by

$$\overline{\boldsymbol{u}} = \frac{1}{N_p N_s}\sum_{i=1}^{N_p}\sum_{j=1}^{N_s}\boldsymbol{u}(t_j,x,Re_i) \qquad\qquad \overline{p} = \frac{1}{N_p N_s}\sum_{i=1}^{N_p}\sum_{j=1}^{N_s}p(t_j,x,Re_i)$$

where N_p is the number of trained Reynolds numbers and N_s the number of snapshots. Two POD bases of dimensions q_u and q_p for the fluctuating velocity and pressure are then constructed and the solutions are approximated as follows

$$\boldsymbol{u}' \approx \sum_{i=1}^{q_u}\alpha_u^i\varphi_u^i \qquad\qquad p' \approx \sum_{i=1}^{q_p}\alpha_p^i\varphi_p^i \tag{13}$$

The above velocity and pressure POD bases were constructed by considering 500 snapshots ($N_s = 500$) regularly distributed between the instants $t_i = 7$ and $t_f = 12$, representing

[8] In this example, the non dimensional Navier-Stokes equations are solved. The variation of the Reynolds number is carried out through the variation of the kinematic viscosity ν. The inlet velocity U in this case is kept constant.

about 8 periods of the flow. The contribution ratio of the k^{th} mode is given by

$$\text{RIC}^k = \sum_{i=1}^{k} \lambda_i / \sum_{i=1}^{N_s} \lambda_i$$

with λ_i the POD eigenvalues. POD eigenvalues and respective modes contribution ratio for the different trained Reynolds number values are represented in figure B.4. It can be noticed that only few modes are capable of reproducing the quasi-totality of the flow. Therefore, for this study case, the POD bases were constructed by considering the 10 first modes for velocity and 8 first modes for the pressure. In what follows, the non intrusive ROM obtained by the proposed method Bi-CITSGM is compared to the ROM obtained by ITSGM/Galerkin. The Galerkin based reduced order model construction for this problem is given in Appendix B.

5.3. Application of the Bi-CITSGM to predict the flow for untrained Reynolds number values

For different untrained Reynolds number values, the *Bi-CITSGM* method is applied to find an approximation of the solutions snapshots of both velocity and pressure. Cubic spline method is used to interpolate the singular values, whilst ITSGM is used for bases interpolation. In a fist attempt to closely Analise the results of the Bi-CITSGM approach, the sensibility of this last with respect to the parameter stepping size ΔRe (length between the points of the sampling points) and the number of neighboring bases N_b considered in the ITSGM, is first investigated. To this end, we considered two examples of untrained Reynolds number values, $Re = 160$ (see Figure B.5) and $Re = 280$ (see Figure B.6). After inspecting the relative mean errors [9] for different configurations combining $N_b \in \{2, 3, 4, 5, 6\}$ and $\Delta Re \in \{20, 30, 40, 50\}$, we observed that there is no specific rule that allows us to have a prior knowledge of the best balance between N_b and ΔRe. Thus in the present article, we have chosen to consider N_b and ΔRe relatively small. That is, $N_b = 3$ and $\Delta Re = 30$ which means that $Re \in \{90, 120, 150, \ldots, 420, 450\}$. The inverse weights powers m and l are chosen such as $m = l = 3$.

Consider now the case of an untrained Reynolds number value $Re = 195$. The associated first four POD and Bi-CITSGM basis functions are represented in figures B.7 and B.8. From a visual point of view, the Bi-CITSGM spatial modes look almost identical to the original POD modes. The quality of the corresponding temporal modes can be checked out by inspecting the hydrodynamics coefficients. These are shown in Figure B.9 and table B.2 where a good match with the coefficients obtained by the high fidelity model can be seen. This agreement is further confirmed by relative errors where the Bi-CITSGM presented a low error of about 0.4% for velocity and 3.2% for pressure. In terms of computational time, table B.3 reports that the proposed Bi-CITSGM performs in real time (less than one second) and is about 10 times faster than the ITSGM/Galerkin approach. This is essentially due to the costly computational operations involved in the Galerkin projection process which are note present in the Bi-CITSGM.

Now, in order to further inspect the robustness of the Bi-CITSGM, the same previous study for $Re = 195$ was performed for several other untrained Reynolds number values. To this end we considered two different regimes, the interpolatory regime lying in the interval $]90, 450[$ and the extraolatory regime lying in the interval $]450, 500[$. In figure B.10, the hydrodynamics coefficients $\overline{C}_D$, $C_{L,max}$, $C_{L,rms}$ and Strouhal number S_t obtained by ITSGM/Galerkin

[9] Let f be a function and $\widetilde{f}$ its approximation, the mean relative error is calculated as follows

$$\bar{\varepsilon}^{\%} = 100 \times \int_0^T ||f - \widetilde{f}||_{L^2(\Omega)}\, dt \Big/ \int_0^T ||f||_{L^2(\Omega)}\, dt$$

and Bi-CITSGM are compared to those obtained by the high fidelity model. Good agreements can be seen for $C_{L,max}$, $C_{L,rms}$ and S_t, whilst it was difficult to track the mean drag coefficient $\overline{C}_D$. In spite of this, reasonably accurate predictions of the flow allover the untrained Reynolds number values have been produced by the Bi-ITSGM. This is shown in Figure B.11 where the recorded mean relative errors are less than 1.5% for velocity and 10% for pressure, in both the interpolatory and extraolatory regimes.

6. Conclusions

In this article, we proposed the non intrusive method Bi-CITSGM for model reduction of parametrized nonlinear time-dependent physical problems. Based on data only, the ability of this approach to quickly and accurately reproduce flow solutions for new untrained parameter values was numerically investigated. To this end, the interpolation and exrapolation cases of the flow past a circular cylinder were considered, where the varied parameter is the Reynolds number. The results show the ability of the Bi-CITSGM to produce reasonably accurate results with a relative mean error less than 1.5% for velocity and 10% for the pressure. Moreover, they show the advantageous computational time of the Bi-CITSGM (less than 1 second) which is reduced by one order of magnitude with respect to the ITSGM/Galerkin, and by several orders of magnitude with respect to the high fidelity model. Future work includes applying the Bi-CITSGM approach on Smolyak grids to more realistic scenarios (experimental data), and use it with a genetic algorithm to solve inverse problems.

Acknowledgement

This material is based upon work financially supported by the Nouvelle-Aquitaine region and CPER/FEDER bâtiment durable.

Appendix A. Review of POD

Let $\boldsymbol{S} \in \mathbb{R}^{N_x \times N_s}$ be the snapshot matrix represented in the low dimensional subspace span(φ) obtained by the POD method. Here, the POD basis can be chosen to be optimal with respect to any inner product. Assume that optimality is realized with respect to an inner product [10] for which the associated linear operator is denoted $\mathcal{A}$. The POD method consists of the following steps

step 1 build the correlation matrix C as $C = \boldsymbol{S}^T \mathcal{A} \boldsymbol{S}$

step 2 solve the eigenvalue problem $C\Lambda = \Lambda\lambda$

step 3 calculate the POD left singular vectors as $\varphi = \boldsymbol{S}\Lambda\lambda^{-\frac{1}{2}}$

Let $\Sigma = \lambda^{\frac{1}{2}}$, the snapshots matrix $\boldsymbol{S}$ can be written as

$$\boldsymbol{S} = \varphi \Sigma \Lambda^T$$

In applications, the POD basis is truncated to an order $q < N_s$, where only the first modes corresponding the the first q significant eigenvalues of C are considered. This truncated basis is sufficient to represent the most of the information contained in $\boldsymbol{S}$.

[10] Different choices can be made for the inner product of optimality of the POD basis. For example, if the POD basis is to be optimal with respect to the L^2 inner product, the operator $\mathcal{A}$ is the mass matrix. The simplest choice is the Euclidean inner product for which $\mathcal{A}$ is the identity matrix.

Appendix B. POD reduced order model of the flow past a cylinder

By plugging expressions (13) into equations (12) and imposing the orthogonality condition of the residual on the basis functions φ_u^i and on the gradient of φ_p^l, the reduced order model associated to the problem of flow past a cylinder writes

$$\begin{cases} \displaystyle\sum_{j=1}^{q_u} M_{ij}^{(u)} \frac{d\alpha_u^j}{dt} + \sum_{j=1}^{q_u} \left[\frac{1}{Re} R_{ij}^{(u)} + \overline{C}_{ij}^{(u)} \right] \alpha_u^j + \sum_{j=1}^{q_u}\sum_{k=1}^{q_u} C_{ijk}^{(u)} \alpha_u^j \alpha_u^k + \sum_{l=1}^{q_p} K_{il}^{(u)} \alpha_p^l = \widetilde{\boldsymbol{F}}_i^{(u)}, \\ \displaystyle\sum_{j=1}^{q_u} M_{mj}^{(p)} \frac{d\alpha_u^j}{dt} + \sum_{j=1}^{q_u} \left[\frac{1}{Re} R_{mj}^{(p)} + \overline{C}_{mj}^{(p)} \right] \alpha_u^j + \sum_{j=1}^{q_u}\sum_{k=1}^{q_u} C_{mjk}^{(p)} \alpha_u^j \alpha_u^k + \sum_{l=1}^{q_p} K_{ml}^{(p)} \alpha_p^l = \widetilde{\boldsymbol{F}}_m^{(p)} \\ \displaystyle\sum_{j=1}^{q_u} M_{ij}^{(u)} \alpha_u^j(0) = \int_\Omega \boldsymbol{u_0} \varphi_u^i \, dx \\ \forall i = 1, \cdots, q_u, \quad \forall m = 1, \cdots, q_p \end{cases} \tag{B.1}$$

where

$$M_{ij}^{(u)} = \int_\Omega \varphi_u^j \varphi_u^i \, dx \qquad R_{ij}^{(u)} = \int_\Omega \nabla\varphi_u^j : \nabla\varphi_u^i \, dx \qquad K_{il}^{(u)} = \int_\Gamma \varphi_p^l \varphi_u^i \cdot \boldsymbol{n} \, d\sigma$$

$$\overline{C}_{ij}^{(u)} = \int_\Omega (\overline{\boldsymbol{u}} \cdot \nabla)\varphi_u^j \cdot \varphi_u^i \, dx + \int_\Omega (\varphi_u^j \cdot \nabla)\overline{\boldsymbol{u}} \cdot \varphi_u^i \, dx$$

$$C_{ijk}^{(u)} = \int_\Omega (\varphi_u^j \cdot \nabla)\varphi_u^k \cdot \varphi_u^i \, dx \qquad \widetilde{\boldsymbol{F}}_i^{(u)} = \int_\Omega \left(\frac{1}{Re} \Delta\overline{\boldsymbol{u}} - \overline{\boldsymbol{u}} \cdot \nabla\overline{\boldsymbol{u}} - \nabla\overline{p} \right) \varphi_u^i \, dx$$

$$M_{mj}^{(p)} = \int_\Omega \varphi_u^j \nabla\varphi_p^m \, dx \qquad R_{mj}^{(p)} = -\int_\Omega \Delta\varphi_u^j : \nabla\varphi_p^m \, dx \qquad K_{ml}^{(p)} = \int_\Omega \nabla\varphi_p^l \nabla\varphi_p^m \, dx$$

$$\overline{C}_{mj}^{(u)} = \int_\Omega (\overline{\boldsymbol{u}} \cdot \nabla)\varphi_u^j \cdot \nabla\varphi_p^m \, dx + \int_\Omega (\varphi_u^j \cdot \nabla)\overline{\boldsymbol{u}} \cdot \nabla\varphi_p^m \, dx$$

$$C_{mjk}^{(p)} = \int_\Omega (\varphi_u^j \cdot \nabla)\varphi_u^k \cdot \nabla\varphi_p^m \, dx \qquad \widetilde{\boldsymbol{F}}_m^{(p)} = \int_\Omega \left(\frac{1}{Re} \Delta\overline{\boldsymbol{u}} - \overline{\boldsymbol{u}} \cdot \nabla\overline{\boldsymbol{u}} - \nabla\overline{p} \right) \nabla\varphi_p^m \, dx$$

More details about this reduced order model can be found in [28].

References

[1] M. Athanasopoulos, H. Ugail, and G. G. Castro, "Parametric design of aircraft geometry using partial differential equations," *Advances in Engineering Software*, vol. 40, no. 7, pp. 479 – 486, 2009.

[2] M. I. G. Bloor and M. J. Wilson, "Efficient parametrization of generic aircraft geometry," *Journal of Aircraft*, vol. 32, pp. 1269–1275, 11 1995.

[3] A. Milišić, Vuk; Quarteroni, "Analysis of lumped parameter models for blood flow simulations and their relation with 1d models," *ESAIM Mathematical Modelling and Numerical Analysis*, vol. 38, pp. 613–632, 07 2004.

[4] W. LU, Y. TIAN, and P. LIU, "Aerodynamic optimization and mechanism design of flexible variable camber trailing-edge flap," *Chinese Journal of Aeronautics*, vol. 30, no. 3, pp. 988 – 1003, 2017.

[5] M. Bergmann and L. Cordier, "Optimal control of the cylinder wake in the laminar regime by trust-region methods and POD reduced-order models," *Journal of Computational Physics*, vol. 227, pp. 7813–7840, 2008.

[6] A. Tallet, C. Allery, and C. Leblond, "Optimal flow control using a POD-based reduced-order model," *Numerical Heat Transfer Part B Fundamentals*, pp. 1–24, 06 2016.

[7] A. Tallet, C. Allery, and F. Allard, "POD approach to determine in real-time the temperature distribution in a cavity," *Building and Environment*, vol. 93, pp. 34–49, 11 2015.

[8] G. Berkooz, P. Holmes, and J. L. Lumley, "On the relation between low-dimensional models and the dynamics of coherent structures in the turbulent wall layer," *Theoretical and Computational Fluid Dynamics*, vol. 4, pp. 255–269, 09 1993.

[9] C. W. Rowley, T. Colonius, and R. M. Murray, "Model reduction for compressible flows using pod and galerkin projection," *Physica D: Nonlinear Phenomena*, vol. 189, no. 1, pp. 115 – 129, 2004.

[10] D. Amsallem and C. Farhat, "An interpolation method for adapting reduced-order models and application to aeroelasticity," *AIAA Journal*, pp. 1803–1813, 2008.

[11] M. Oulghelou and C. Allery, "Aip conference proceedings [author(s) icnpaa 2016 world congress: 11th international conference on mathematical problems in engineering, aerospace and sciences - la rochelle, france (4–8 july 2016)] - optimal control based on adaptive model reduction approach to control transfer phenomena," vol. 1798, 2017.

[12] M. Oulghelou and C. Allery, "A fast and robust sub-optimal control approach using reduced order model adaptation techniques," *Applied Mathematics and Computation*, vol. 333, pp. 416 – 434, 2018.

[13] D. Xiao, P. Yang, F. Fang, J. Xiang, C. Pain, and I. Navon, "Non-intrusive reduced order modelling of fluid–structure interactions," *Computer Methods in Applied Mechanics and Engineering*, vol. 303, 05 2016.

[14] D. Xiao, F. Fang, C. Pain, and I. Navon, "A parameterized non-intrusive reduced order model and error analysis for general time-dependent nonlinear partial differential equations and its applications," *Computer Methods in Applied Mechanics and Engineering*, vol. 317, pp. 868 – 889, 2017.

[15] V. Shinde, E. Longatte, F. Baj, Y. Hoarau, and M. Braza, "A galerkin-free model reduction approach for the Navier-Stokes equations," *Journal of Computational Physics*, vol. 309, pp. 148 – 163, 2016.

[16] M. Joyner, "Comparison of two techniques for implementing the Proper orthogonal decomposition method in damage detection problems," *Mathematical and Computer Modelling*, vol. 40, 2004.

[17] A. Srivastava and E. Klassen, "Bayesian and geometric subspace tracking," *Advances in Applied Probability*, vol. 36, pp. 43–56, 03 2004.

[18] M. T. Harandi, C. Sanderson, S. Shirazi, and B. C. Lovell, "Graph embedding discriminant analysis on Grassmannian manifolds for improved image set matching," in *CVPR 2011*, pp. 2705–2712, June 2011.

[19] M. Harandi, R. Hartley, M. Salzmann, and J. Trumpf, *Dictionary Learning on Grassmann Manifolds*, pp. 145–172. Cham: Springer International Publishing, 2016.

[20] H. Cetingul and R. Vidal, "Intrinsic mean shift for clustering on Stiefel and Grassmann manifolds," 2009.

[21] A. Edelman, T. A. Arias, and S. T. Smith, "The geometry of algorithms with orthogonality constraints," *SIAM Journal on Matrix Analysis and Applications*, vol. 20, pp. 303–353, 01 1998.

[22] A. Absil, R. Mahony, and R. Sepulchre, "Riemann geometry of Grassmann manifolds with a view on algorithmic computation," *Acta Applicandae Mathematicae*, vol. 80, Issue 2, p. 199–220, 2004.

[23] N. Boumal and P.-A. Absil, "Low-rank matrix completion via preconditioned optimization on the Grassmann manifold," *Linear Algebra and its Applications*, vol. 475, pp. 200–239, 06 2015.

[24] R. Wald, "General relativity," *The University of Chicago Press*, 1984.

[25] W. Boothby, "An introduction to differentiable manifolds and riemanniann geometry," *Academic Press*, 2003.

[26] N. T. Son, "A real time procedure for affinely dependent parametric model order reduction using interpolation on grassmann manifolds," *International Journal for Numerical Methods in Engineering*, vol. aop, 2012.

[27] H. P. Langtangen and A. Logg, *Solving PDEs in Python: The FEniCS Tutorial I.* Springer Publishing Company, Incorporated, 1st ed., 2017.

[28] A. Tallet, C. Allery, C. Leblond, and E. Liberge, "A minimum residual projection to build coupled velocity–pressure POD-rom for incompressible Navier-Stokes equations," *Communications in Nonlinear Science and Numerical Simulation*, vol. 22, pp. 909–932, 05 2015.

[29] C. Liu, X. Zheng, and C. Sung, "Preconditioned multigrid methods for unsteady incompressible flows," *Journal of Computational Physics*, vol. 139, no. 1, pp. 35 – 57, 1998.

[30] R. D. HENDERSON, "Nonlinear dynamics and pattern formation in turbulent wake transition," *Journal of Fluid Mechanics*, vol. 352, p. 65–112, 1997.

[31] C. NORBERG, "Flow around a circular cylinder: Aspects of fluctuating lift," *Journal of Fluids and Structures*, vol. 15, no. 3, pp. 459 – 469, 2001.

[32] A. Placzek, J.-F. Sigrist, and A. Hamdouni, "Numerical simulation of an oscillating cylinder in a cross-flow at low reynolds number: Forced and free oscillations," *Computers & Fluids*, vol. 38, no. 1, pp. 80 – 100, 2009.

[33] D. Calhoun, "A cartesian grid method for solving the two-dimensional streamfunction-vorticity equations in irregular regions," *Journal of Computational Physics*, vol. 176, no. 2, pp. 231 – 275, 2002.

List of Figures

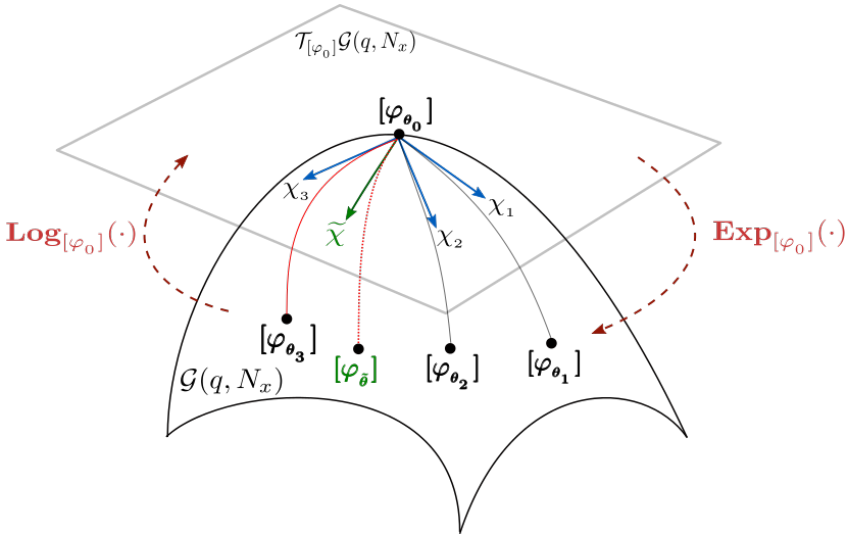

Figure B.1: Illustration of bases interpolation by ITSGM. Step 1 : chose a point of tangency $[\varphi_{\theta_0}]$ and define the tangent space $\mathcal{T}_{[\varphi_0]}\mathcal{G}(q,N)$; Step 2 : compute the initial velocities $\chi_k \in \mathcal{T}_{[\varphi_0]}\mathcal{G}(q,N)$ as the image by the logarithmic mapping of the subspaces $[\varphi_{\theta_k}] \in \mathcal{G}(q,N)$; Step 3 : Interpolate χ_k and obtain the approximate initial velocity $\widetilde{\chi}$ associated the the new untrained parameter $\widetilde{\theta}$; Step 4 : determine the approximate subspace $[\varphi_{\tilde{\theta}}]$ as the image by the exponential mapping of $\widetilde{\chi} \in \mathcal{T}_{[\varphi_0]}\mathcal{G}(q,N)$.

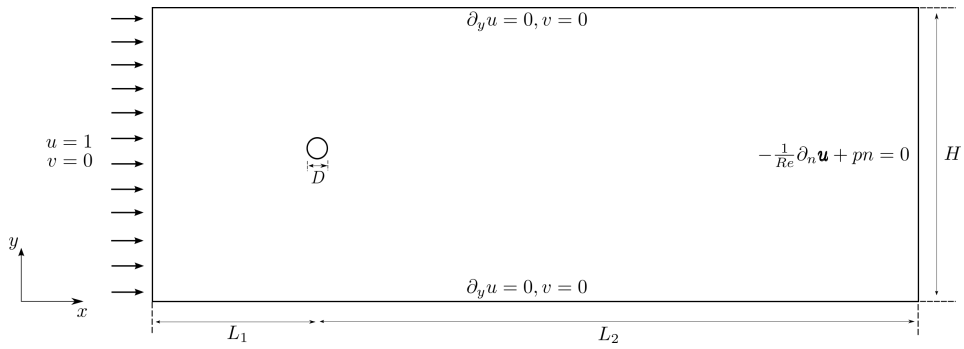

Figure B.2: Two-dimensional domain and boundary conditions for the problem of flow past a circular cylinder.

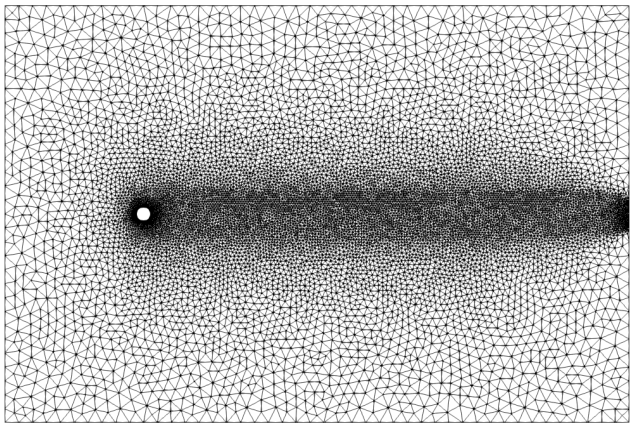

Figure B.3: Non-uniform mesh used to simulate the problem of flow past a circular cylinder.

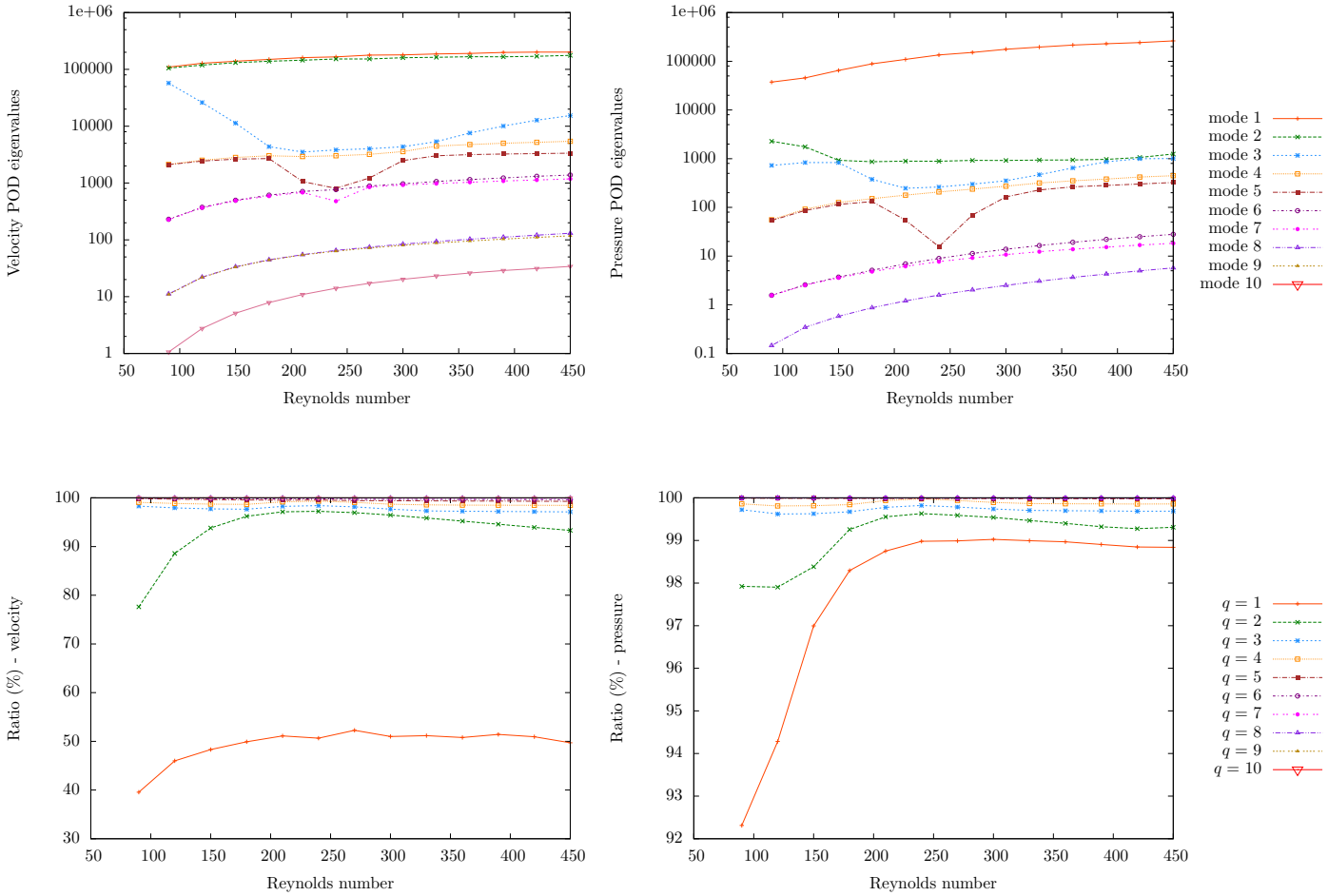

Figure B.4: POD eigenvalues and corresponding ratio with respect to trained Reynolds numbers. q is referred to as the number of POD modes.

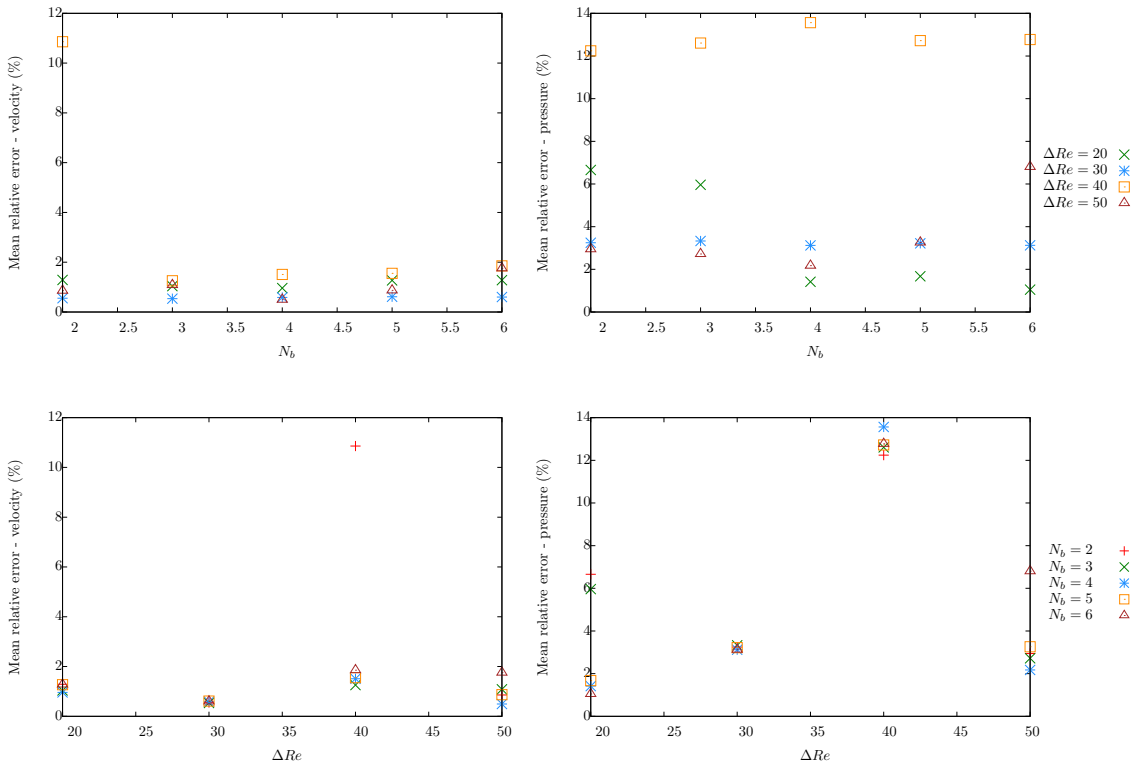

Figure B.5: Influence of the number of neighboring bases N_b and the sampling stepping size ΔRe on the Bi-CITSGM for the untrained value $Re = 160$.

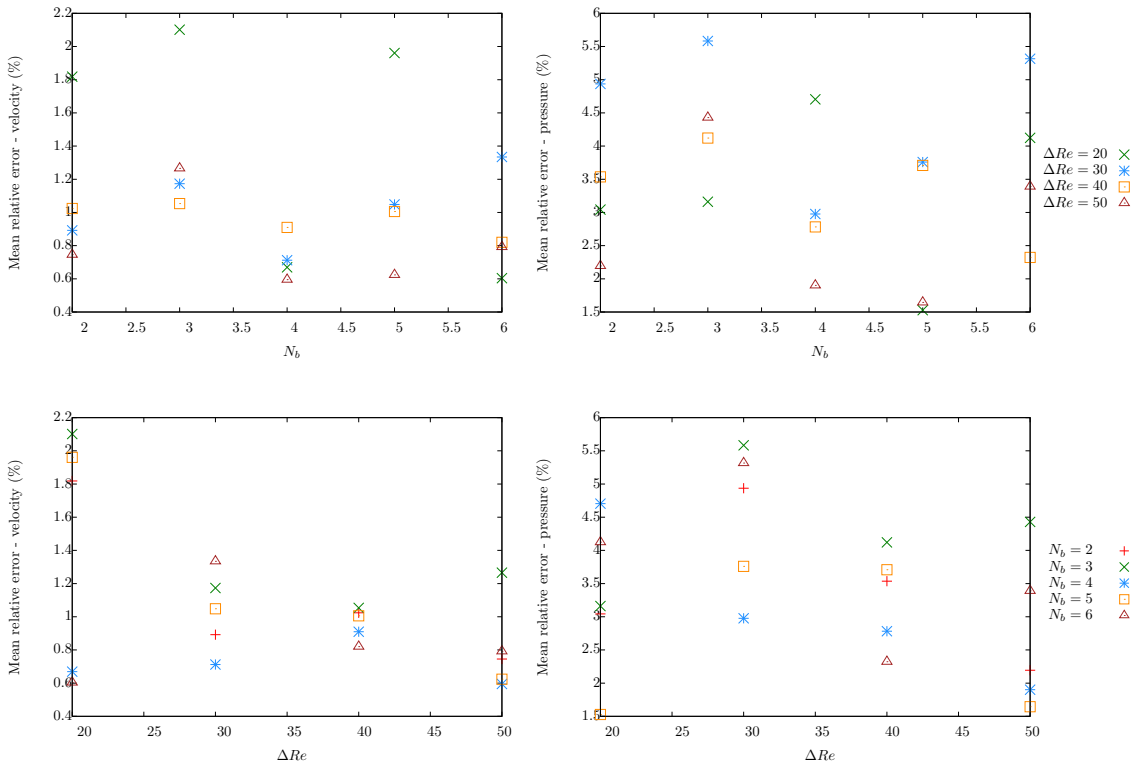

Figure B.6: Influence of the number of neighboring bases N_b and the sampling stepping size ΔRe on the Bi-CITSGM for the untrained value $Re = 280$.

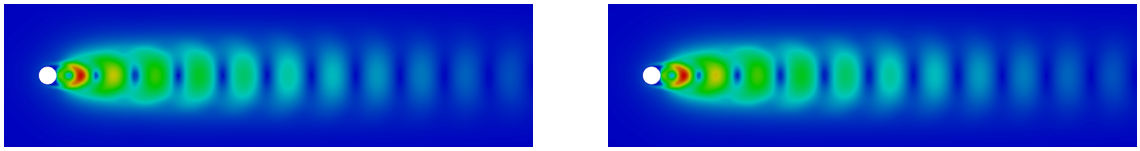

(a) mode 1

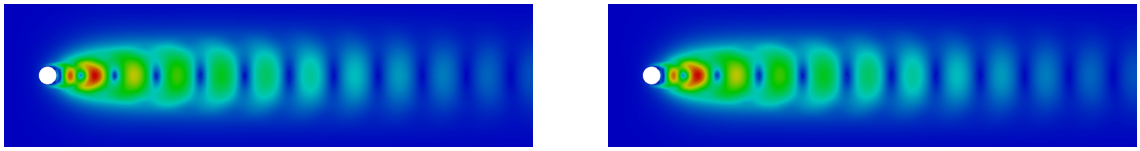

(b) mode 2

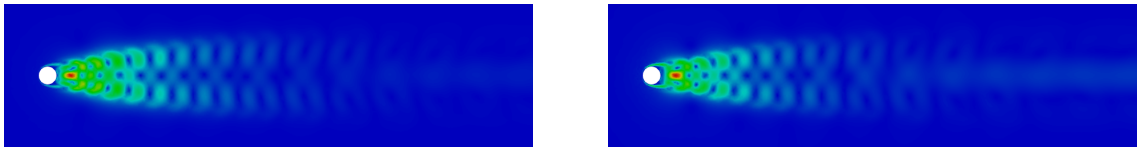

(c) mode 3

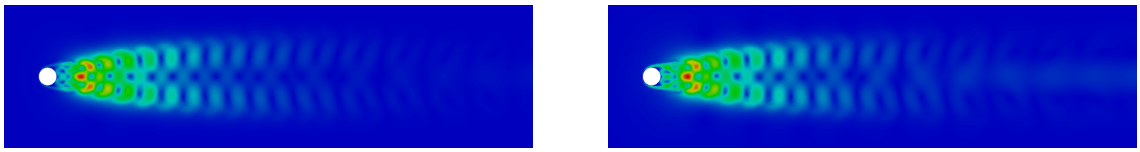

(d) mode 4

Figure B.7: POD (left) and calibrated ITSGM (right) velocity modes associated to the untrained Reynolds number $Re = 195$.

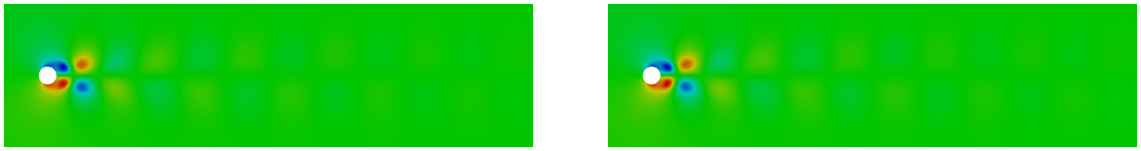

(a) mode 1

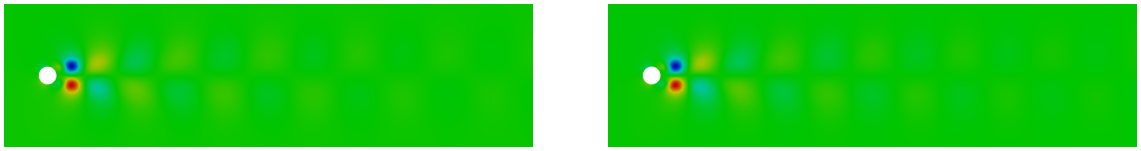

(b) mode 2

(c) mode 3

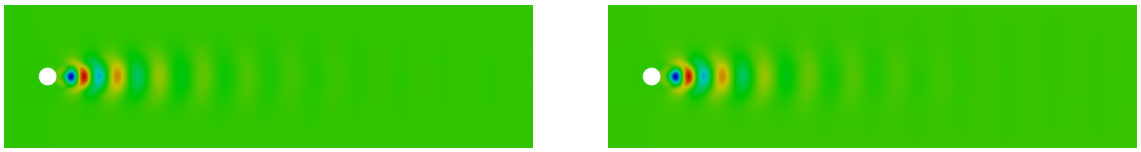

(d) mode 4

Figure B.8: POD (left) and calibrated ITSGM (right) pressure modes associated to the untrained Reynolds number $Re = 195$.

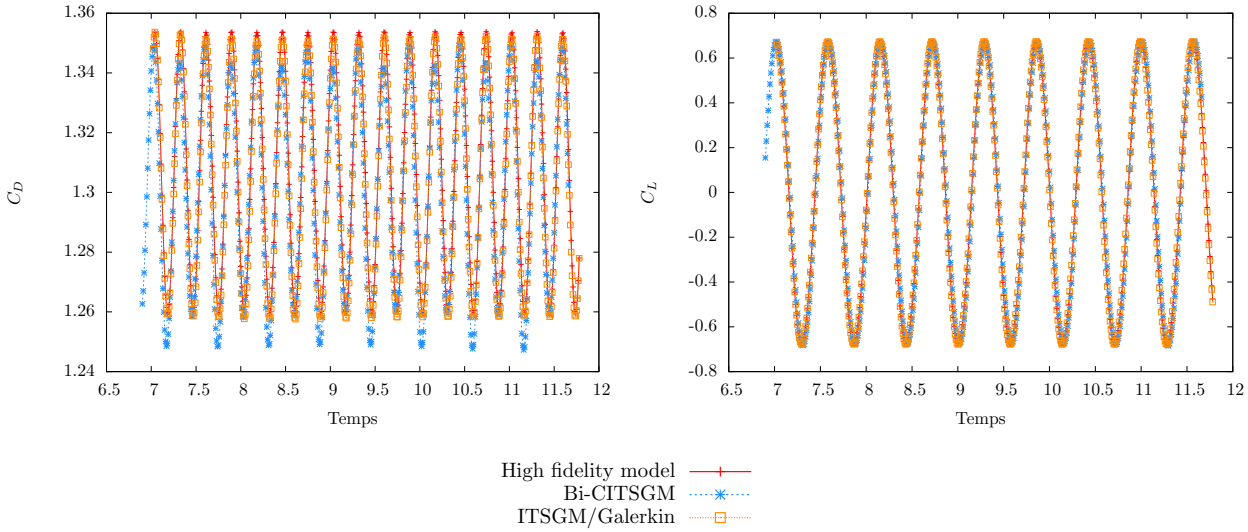

Figure B.9: Lift and drag coefficients C_D and C_L obtained by Bi-CITSGM and ITSGM/Galerkin with those obtained by the high fidelity model at the untrained Reynolds number $Re = 195$.

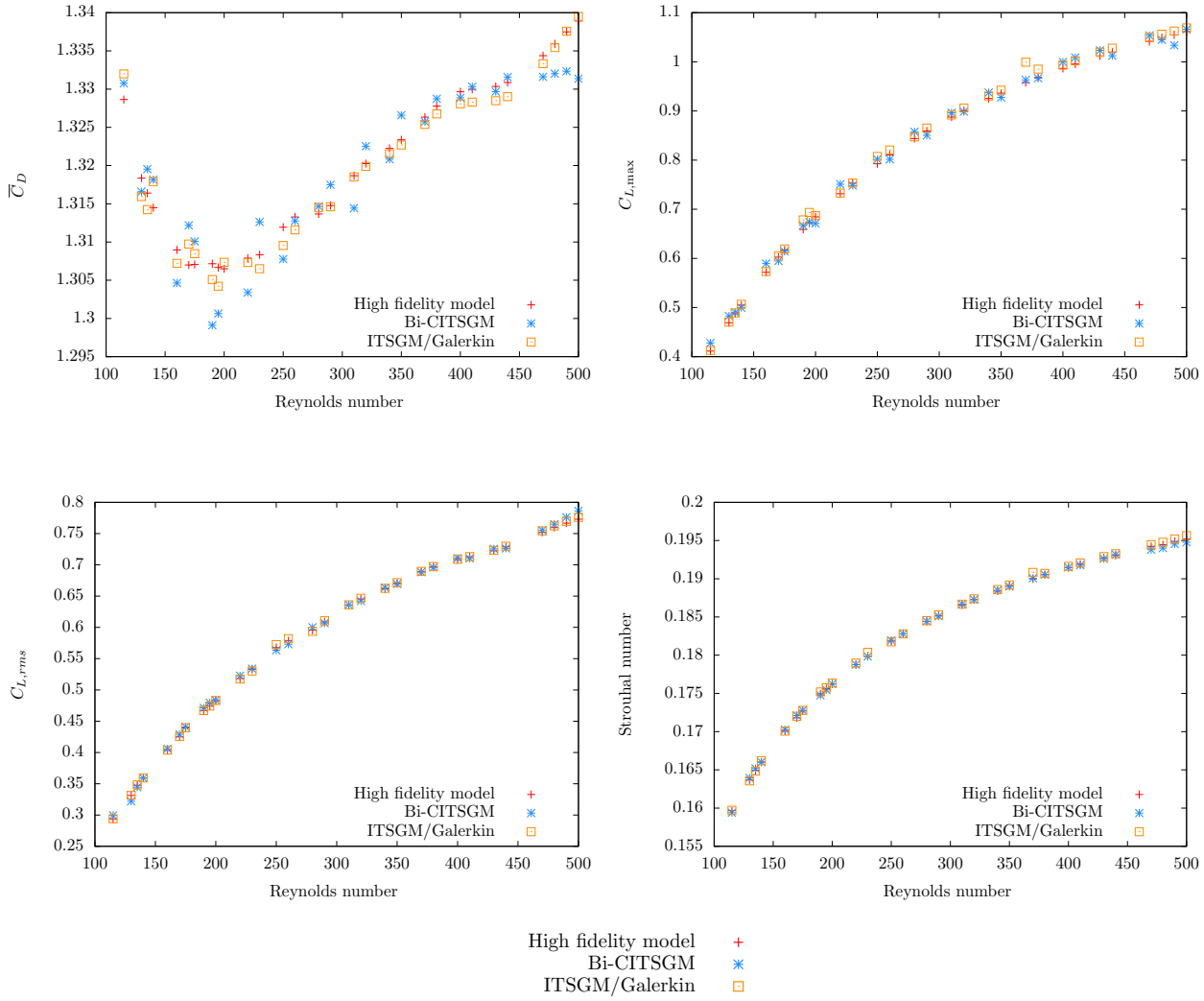

Figure B.10: Aerodynamics coefficient and Strouhal number at different untrained Reynolds number values.

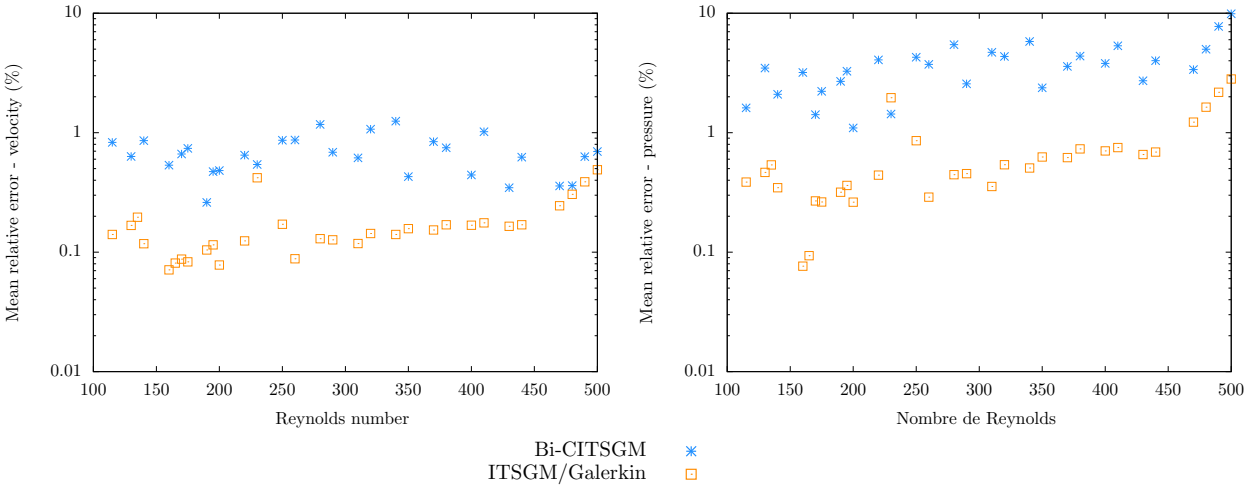

Figure B.11: Mean relative Errors at different untrained Reynolds number values.

List of Tables

Coefficient	Current	Liu [29]	Henderson [30]	Norberg [31]	Placzek [32]	Calhoun [33]
$\overline{C}_D$	1.343	1.350	1.335	-	1.374	1.330
$C_{L,max}$	0.348	0.339	-	-	0.327	0.298
$C_{L,rms}$	0.245	-	-	0.227	0.226	-
S_t	0.154	0.164	0.165	0.164	0.168	0.175

Table B.1: Comparison of the hydrodynamics coefficients and the Strouhal number obtained by the current simulations (Fenics) with those of the literature.

Method	$\overline{C}_D$	$C_{L,max}$	$C_{L,rms}$	S_t	$\overline{\varepsilon}^{\%}_{\boldsymbol{u}}$	$\overline{\varepsilon}^{\%}_{p}$
High fidelity model	1.30	0.67	0.47	0.17	-	-
ITSGM/Galerkin	1.30	0.69	0.47	0.17	0.1%	0.3%
Bi-CITSGM	1.30	0.67	0.48	0.17	0.4%	3.2%

Table B.2: Aerodynamics coefficients and mean relative at the untrained Reynolds number $Re = 195$. $\overline{\varepsilon}^{\%}_{\boldsymbol{u}}$ and $\overline{\varepsilon}^{\%}_{p}$ are respectively velocity and pressure mean relative errors.

ITSGM/Galerkin	Bi-CITSGM
9.5 sec	0.8 sec

Table B.3: Comparison of the computational time of a single prediction needed by the ITSGM/Galerkin approach and the Bi-CITSGM approach.